

Enhanced Self-supervised Learning for Multi-modality MRI Segmentation and Classification: A Novel Approach Avoiding Model Collapse

Linxuan Han, Sa Xiao, Zimeng Li, Haidong Li, Xiuchao Zhao, Fumin Guo, Yeqing Han, Xin Zhou

Abstract—Multi-modality magnetic resonance imaging (MRI) can provide complementary information for computer-aided diagnosis. Traditional deep learning algorithms are suitable for identifying specific anatomical structures segmenting lesions and classifying diseases with magnetic resonance images. However, manual labels are limited due to high expense, which hinders further improvement of model accuracy. Self-supervised learning (SSL) can effectively learn feature representations from unlabeled data by pre-training and is demonstrated to be effective in natural image analysis. Most SSL methods ignore the similarity of multi-modality MRI, leading to model collapse. This limits the efficiency of pre-training, causing low accuracy in downstream segmentation and classification tasks. To solve this challenge, we establish and validate a multi-modality MRI masked autoencoder consisting of hybrid mask pattern (HMP) and pyramid barlow twin (PBT) module for SSL on multi-modality MRI analysis. The HMP concatenates three masking steps forcing the SSL to learn the semantic connections of multi-modality images by reconstructing the masking patches. We have proved that the proposed HMP can avoid model collapse. The PBT module exploits the pyramidal hierarchy of the network to construct barlow twin loss between masked and original views, aligning the semantic representations of image patches at different vision scales in latent space. Experiments on BraTS2023, PI-CAI, and lung gas MRI datasets further demonstrate the superiority of our framework over the state-of-the-art. The performance of the segmentation and classification is substantially enhanced, supporting the accurate detection of small

lesion areas. The code is available at <https://github.com/LinxuanHan/M2-MAE>.

Index Terms—Multi-modality MRI, self-supervised learning, mask image modeling, Transformer.

I. INTRODUCTION

MULTI-MODALITY magnetic resonance imaging (MRI) can provide complementary and mutually informative data about tissue composition (i.e., anatomical or functional information), enabling intuitive insight into the human body's interior. This assists radiologists and clinicians in detecting and treating diseases more efficiently. For example [1], to accurately define the shapes, sizes, and diffused locations of gliomas, the whole tumor (WT) region is highly distinguishable with fluid attenuation inversion recovery (FLAIR), and the enhancing tumor (ET) region exhibits clear structures in T1-weighted contrast-enhanced imaging (T1ce). In recent years, numerous deep learning-based computer-aided diagnosis algorithms have been proposed to fuse modality and extract the features for MRI segmentation and classification. However, these data-driven algorithms, such as U-Net [2] and its variants [3]–[8], require a large dataset with accurate annotations. Medical image annotations are still manually performed by experienced neuro-radiologists, which is extremely tedious and time-consuming. Moreover, the annotation of multi-modality MRI is more difficult to obtain than single-modality MRI.

Self-supervised learning (SSL), semi-supervised learning, and weakly supervised learning are viable deep learning

This work was supported by National key Research and Development Project of China (2018YFA0704000), National Natural Science Foundation of China (82127802, 21921004), Key Research Program of Frontier Sciences (ZDBS-Y-JSC004), the Strategic Priority Research Program of the Chinese Academy of Sciences (grant No. XDB0540000), and Hubei Provincial Key Technology Foundation of China (2021ACA013, 2023BAA021, 2023AFB1061).

L. Han is with the Key Laboratory of Magnetic Resonance in Biological Systems, State Key Laboratory of Magnetic Resonance and Atomic and Molecular Physics, National Center for Magnetic Resonance in Wuhan, Wuhan Institute of Physics and Mathematics, Innovation Academy for Precision Measurement Science and Technology, Chinese Academy of Sciences-Wuhan National Laboratory for Optoelectronics, Huazhong University of Science and Technology, Wuhan 430071, China (e-mail: hanlinxuan@hust.edu.cn).

S. Xiao, Z. Li, H. Li, X. Zhao, and Y. Han are with the Key Laboratory of Magnetic Resonance in Biological Systems, State Key Laboratory of Magnetic Resonance and Atomic and Molecular Physics, National Center for Magnetic Resonance in Wuhan, Wuhan Institute of Physics and Mathematics, Innovation Academy for Precision Measurement Science and Technology, Chinese Academy of Sciences, Wuhan 430071, China, also with the University of Chinese Academy of Sciences, Beijing, 100049, China (e-mail: xiaosa@wipm.ac.cn; zm_li@hust.edu.cn; haidong.li@wipm.ac.cn; xiuchao.zhao@apm.ac.cn; hanyeqing@wipm.ac.cn).

F. Guo is with Wuhan National Laboratory for Optoelectronics, Department of Biomedical Engineering, Huazhong University of Science and Technology, Wuhan 430074, China (e-mail: fguo@hust.edu.cn).

X. Zhou is with the Key Laboratory of Magnetic Resonance in Biological Systems, State Key Laboratory of Magnetic Resonance and Atomic and Molecular Physics, National Center for Magnetic Resonance in Wuhan, Wuhan Institute of Physics and Mathematics, Innovation Academy for Precision Measurement Science and Technology, Chinese Academy of Sciences, Wuhan 430071, China, also with the University of Chinese Academy of Sciences, Beijing, 100049, China, and also with Key Laboratory of Biomedical Engineering of Hainan Province, School of Biomedical Engineering, Hainan University, Haikou 570228, China (e-mail: xinzhou@wipm.ac.cn). (Corresponding author: Xin Zhou.) (Linxuan Han and Sa Xiao contributed equally to this work.)

paradigms for learning image features with reduced requirement of manual annotations [9]-[11]. In SSL, unlabeled data is trained to initialize model parameters through pre-training. These initialization parameters can then be used for supervised learning to enhance the generalization ability of the model for specific tasks. In other words, this method is expected to improve the performance of multi-modality MRI analysis.

SSL can be broadly grouped into contrastive learning and masked image modeling (MIM). Contrastive learning [11]-[14] defines positive pairs (same image with/without augmentation) and negative pairs (different images). Then the encoder is trained by reducing the distance between positive pairs and increasing the distance between negative pairs. However, most contrastive learning methods simply align the positive pairs without using negative pairs, resulting in all data converging to the trivial solution, which is also known as model collapse [15]. MIM masks patches of an image and then reconstructs the masked parts based on unmasked region [16]-[21]. Although latent features do not collapse on natural image datasets [22], [23], there is model collapse when using multi-modality MRI datasets. Fig. 1 illustrates the performance of reconstructing masked patches using MIM on the BraTS2023 dataset. The patches reconstructed by MIM generate low-frequency information (such as the shape of the whole brain) but lack high-frequency information (such as the texture of tissues and tumors) in the pre-training stage [24]. In other words, the reconstruction process exhibits “averaging” effect of voxel signal intensities (as shown in the bottom row of Fig. 1), which may hinder the following segmentation and classification tasks.

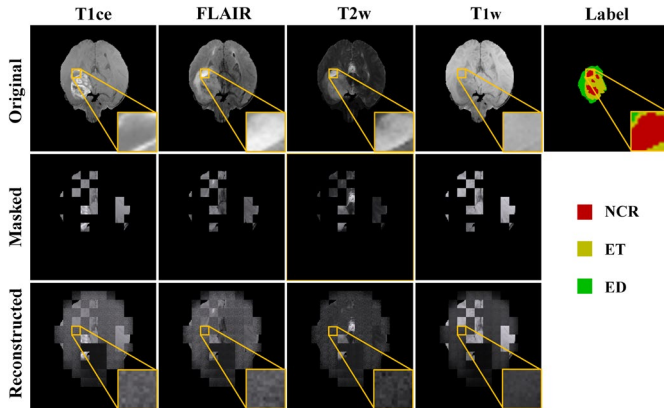


Fig. 1. Example result of one MRI scan from BraTS2023 [1] validation set. As the original images are all 3D volumes, reconstructed images are shown in the form of slices. The necrotic tumor core (NCR), enhancing tumor (ET), and edematous tissue (ED) are presented in red, yellow, and green respectively, in the last column. Each row corresponds to one example. For each modality, the original images (top), the masked images (middle), and the MIM reconstruction patches (bottom) are shown. In this case, a Vision Transformer-based backbone is applied to the encoder, and the masking ratio is 75%.

In this work, we investigate the mechanism of model collapse in MIM when using multi-modality MRI datasets and provide a solution (see Section III for detail) to minimize this critical issue. Particularly, multi-modality MRI datasets are non-iconic (iconic means that each image in the dataset can be classified into a certain category) and have high similarity. In other words, the proportion of background, which has minimal contribution to segmentation and classification tasks in the multi-modality

MRI datasets, is larger; the proportion of target organs and lesions, which is highly relevant to segmentation and classification tasks, is smaller. As a result, when MIM is applied directly, the lower bound of training loss can be small, leading to model collapse in multi-modality MRI datasets. Therefore, improving the lower bound of training loss may avoid model collapse and here we propose to address this issue by designing a new masking strategy.

We propose a Multi-modality MRI Masked Autoencoder (M^2 -MAE), including a novel masking strategy and a correspondingly adapted model architecture that facilitates the masking strategy. Hybrid mask pattern (HMP) has been designed to improve the lower bound of training loss to avoid model collapse. HMP connects three masking steps, masking multi-modality MRI at the modality, position, and patch level, forcing the model to learn semantic connection of image representations by reconstructing masking information in the pre-training stage. To adapt HMP for downstream voxel-level dense prediction tasks, pyramid barlow twin (PBT) module is designed to further ensure stability and apply targets at different vision scale. The PBT module aligns semantic representations between masked and original views in the pre-training stage, which implements feature pyramid in the encoder in the pre-training stage using barlow twin loss in low-level feature. In addition, we replace the entire decoder with a single projection head on model architecture to reduce computational complexity and increase the capability of the encoder. Finally, the performance of segmentation and classification tasks is enhanced through M^2 -MAE.

Our main contributions can be summarized as follows:

- 1) We investigate the mechanism of model collapse in current self-supervised learning of multi-modality MRI and design a novel HMP that can effectively avoid model collapse.
- 2) We propose a PBT module to align features extracted from the masked and original images at different vision scale in the latent space during the pre-training stage. It regularizes the modality reconstruction process compared to typical SSL method.
- 3) Semi-supervised learning tasks are constructed using the pre-training weight with large amount of unlabeled data. Experimental results show that, the model performs similarly to a fully supervised model with only 60% of the data labeled.
- 4) The proposed M^2 -MAE has been validated on three multi-modality MRI datasets. The results demonstrate that our model can handle various segmentation and classification tasks. It has achieved state-of-the-art performance in self-supervised learning works. The generalization ability and robustness of the strategy are also extensively investigated.

II. RELATED WORK

A. Multi-modality MRI Analysis

So far, many deep learning based multi-modality MRI analysis methods have been proposed. For instance, Schelb *et al.* [25] trained a U-Net with T2-weighted and diffusion MRI to segmented prostate cancer. Based on U-Net, several networks, such as TransUNet [3],[26] and UNETR [4] employing vision

transformer (ViT), have been proposed to improve the segmentation performance on BraTS2020. Yang *et al.* [27] designed a dual disentanglement network for brain tumor segmentation with missing modalities. Chen *et al.* [28] proposed a modality-specific information disentanglement framework to extract inter- and intra-modality attention maps on multi-modality MRI. Liang *et al.* [29] employed a 3D Dense Net model to predict Isocitrate Dehydrogenase (IDH) genotypes with all tumor lesion patches. Furthermore, Cheng *et al.* [30] combined the tasks of glioma genotyping and segmentation into a multi-task network on BraTs2020. In addition, Li *et al.* [31] proposed a complementation-reinforced network to reconstruct and segment the pulmonary gas MRI.

B. Self-supervised Learning

Supervised learning methods mentioned above rely on fully annotated medical datasets. As a viable alternative, self-supervised learning obtains supervisory signals from given data and learns generalizable dense representations of the input. There are two main directions in self-supervised learning.

The first direction is contrastive learning [9],[32]-[34], which defines positive and negative sample pairs as learning tasks and treats them differently in the loss function. Marin *et al.* [32] pre-trained the ResNet50 backbone for object detection in chest X-ray. Zheng *et al.* [9] proposed a multiscale visual representation learning algorithm to perform finer-grained representation and to handle different target scales for downstream segmentation tasks. Together with the contrast loss, Zhou *et al.* [33] presented preservation contrastive learning for self-supervised medical representations. Moreover, Jiang *et al.* [34] designed a conditional anatomical feature alignment module to complement corrupted embeddings with globally matched semantics to create contrastive pairs in 3D medical analysis.

The other direction is MIM [21],[24],[35],[36], such as masked autoencoders (MAE), which represent the state-of-the-art (SOTA) on natural datasets. Yan *et al.* [35] proposed a privacy-preserving and federated self-supervised learning framework that collaboratively trained models on decentralized data using masked image modeling as the self-supervised task. Chen *et al.* [21] employed masked image modeling approaches to advance 3D medical image analysis using a lightweight decoder for reconstruction. Haghighi *et al.* [36] developed a framework that united discriminative, restorative, and adversarial learning in a unified manner. Yan *et al.* [24] proposed a hybrid visual representation learning framework for self-supervised pre-training on large unlabeled medical datasets using contrastive and generative modelling.

C. Model Collapse

Self-supervised learning that maps similar data to close spots in the representation space could lead to the collapsing problem. This means that all outputs tend to collapse to a constant feature. Some studies have introduced new self-supervised frameworks to avoid model collapse. For example, LeCun *et al.* [20] measured the cross-correlation matrix between the outputs of two identical networks called Barlow Twins. Zhang *et al.* [37] presented a new approach termed align representations with

base (ARB), which aligns the learned embeddings to intermediate variables. Compared to Barlow Twins, ARB does not require pairwise decorrelation, resulting in linear complexity. Also, some researchers attempted to avoid model collapse by redesigning proxy tasks and loss function. Wang *et al.* [38] employed a network ended with a SoftMax operation to produce twin-class distributions of two augmentation images. Moon *et al.* [39] used the same random vector for the augmented embeddings of the given image. This implies that the embeddings are locally dispersed, giving a latent contrast effect between the embeddings of different images. Zhang *et al.* [23] established a close connection between MAE and contrastive learning and showed that MAE implicitly aligns the mask-induced positive pairs. They proposed a uniformity-enhanced MAE loss that can address model collapse.

III. METHODS

A. Model Collapse on Multi-modality MRI

In this work, we investigate the reason why traditional masked strategy of SSL leads to model collapse in multi-modality MRI. For clarification, we define the following notations: $D_L = \{(x^i, g^i, y^i)\}_{i=1}^{N_L}$ is a labeled dataset with N_L samples, where $x^{(i)}$ is the image of the i -th sample in input multi-modality MRI, $y^i \in \{0,1\}$ denotes the class of the i -th sample, and g^i represents the corresponding ground truth segmentation.

It is known that, in contrastive learning, simply aligning positive pairs will result in full model collapse because the alignment loss can be minimized by the encoder [18]. MIM methods do not suffer from model collapse on natural image datasets during pre-training [23]. However, when directly applying MIM to multi-modality MRI datasets, model collapse occurs in pre-training due to the similarity of multi-modality MRI. Here, we theoretically investigate the issue of model collapse in MIM for MR images.

In MIM, an MR image x from D_L is divided into n patches $R^{n \times s}$, e.g., $x \in R^{n \times s}$, where s denotes the patch size. Next, a random binary mask $m \in \{0, 1\}^n$ is drawn with probability as the mask ratio ρ (the ratio of removed patches), two complementary masked views of x are obtained:

$$x_m = x[m] \in R^{n_1 \times s}, \quad x_t = x[1-m] \in R^{n_2 \times s} \quad (1)$$

where $n_1 = n \times (1 - \rho)$, $n_2 = n \times \rho$ are integers satisfying $n = n_1 + n_2$. An MAE essentially learns to pair the two complementary views x_m and x_t via the reconstruction task, which can be modeled by a bipartite graph. Let $X_m = \{x_m\}$ and $X_t = \{x_t\}$ denote the set of all masked and target views, respectively. Each view $x \in X$ is considered as a node. Accordingly, there is an edge between two views when they are complementary views generated by masking.

MIM produces latent connections among different input samples in the form of 2-hop connectivity [22]. Given a pair of 2-hop input neighbors $x_m^1, x_m'^1 \in X_m$ that share a common complementary target view $x_t^1 \in X_t$, by enforcing $x_m^1, x_m'^1$ to reconstruct the same output x_t^1 , MIM implicitly pulls their

features together [shown in Fig. 2. (a)]. For two points $x_m^1, x_m^3 \in X_m$, that have a similar reconstruction target $x_t^1 \in X_t$ (more likely to happen under a larger mask ratio ρ) [shown in Fig. 2. (b)], are also pulled together by MIM. The 2-hop input neighbors are positive pairs that implicitly align as in contrastive learning. Then, the reconstruction loss of MIM [23] can be lower bounded by the alignment loss between positive pairs:

$$\mathcal{L}_{\text{MIM}}(x) \geq -\frac{1}{2} \mathbb{E}_{x_m, x_m^+} M(x_m)^\top M(x_m^+) - \varepsilon + \text{const} \quad (2)$$

where x_m^+ denotes a positive masked view of x_m , and $M(\cdot)$ indicates the MIM model operates on masked images. When the encoder fully collapses, $\forall x_m \in X_m, f(x) = c$, the MAE loss has a large lower bound:

$$\mathcal{L}_{\text{MIM}} \geq \text{Var}(X_t) \quad (3)$$

where $\text{Var}(X_t)$ denotes the variance of masked targets X_t computed on the training dataset.

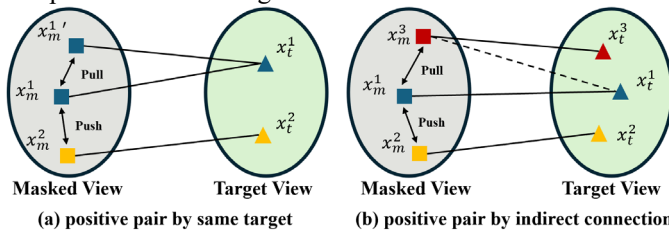


Fig. 2. The bipartite graph is divided into (a) positive pair by the same target and (b) positive pair by indirect connection. Then, the reconstruction task of MIM is transformed as contrastive task.

As there are multiple classes and diverse styles in natural dataset, such as CIFAR-10 [40], the $\text{Var}(X_t)$ and lower bound of train loss are relatively high. Thus, the train loss cannot be minimized by a collapsed encoder on pre-training stage. In contrast, the appearance and styles of multi-modality MR images are similar due to registration, cropping and standardization in the pre-processing stage. Therefore, the $\text{Var}(X_t)$ and the lower bound of train loss are relatively low, which often times leads to a collapsed encoder when minimizing the loss. Accordingly, the pre-training encoder cannot effectively learn image features, and the reconstructed images lack discrimination, resulting in poor performance of downstream segmentation and classification tasks.

Monte Carlo sampling is used to calculate the $\text{Var}(X_t)$ under CIFAR-10, BraTS2023, PI-CAI, lung gas MRI (LungasMRI) datasets by masking image with different masking ratios. As shown in Fig. 3, the variance of natural dataset (CIFAR-10) is much higher than that on the BraTS2023, PI-CAI and LungasMRI datasets, leading to model collapse on pre-training.

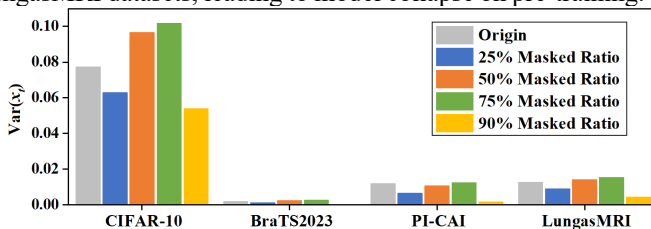


Fig. 3. Result of Monte Carlo sampling of calculating $\text{Var}(X_t)$ with different mask ratios on the CIFAR-10, BraTS2023, PI-CAI, and LungasMRI datasets. The variance of CIFAR-10 reaches its maximum with a 75% masking ratio, which is similar to the trend of the MAE performance [19].

B. Multi-modality MRI Masked Autoencoder

Here, multi-modality masked autoencoder (M^2 -MAE) is proposed to address the model collapse issue. As shown in Fig. 4, M^2 -MAE uses a masked image reconstruction model as the backbone of the self-supervised learning module for multi-modality MRI. M^2 -MAE is composed of hybrid mask pattern (HMP) as the masking strategy and a pyramid barlow twin (PBT) module. M^2 -MAE masks the multi-modality MR images and trains the encoder by reconstructing the masked patches, then the pre-trained encoder is applied to downstream segmentation and classification tasks.

In M^2 -MAE, input images X are masked by HMP to get X_m , firstly. X and X_m are then separately entered into two vision Transformer-based encoders E_{ViT} . Note that the encoders E_{ViT} are responsible for modeling latent feature representations of the masked patches, which are used to reconstruct the original image patches in the masked area. As a standard ViT, the encoders of M^2 -MAE embed patches through linear projection with the incorporation of positional embeddings and processes the resulting features via a series of Transformer blocks. The shared weights of encoders E_{ViT} operate on both the masked and unmasked patches of the entire dataset, which produce embedding Z and Z_m for input and masked images, respectively. Thirdly, the embedding of each transformer block is fed to a PBT module to align features of the masked images and the input images at various scales.

Lastly, Z_m from E_{ViT} are reconstructed by a decoder and a discriminator via adversarial learning. The input to the decoder is the full set of tokens consisting of encoded visible patches. A lightweight decoder reduces computational complexity and increases the ability of encoder to learn more generalizable representations that the decoder can quickly grasp, translate, and convey [26]. The encoder is more critical because the decoder is only used during pre-training to perform the image reconstruction task (only the encoder is used to produce image representations for recognition). Therefore, the entire decoder is replaced with a single output projection $g(\cdot)$ in M^2 -MAE.

1) Hybrid Mask Pattern

To alleviate model collapse in MIM, a novel masking strategy (HMP) is designed for multi-modality MRI to improve $\text{Var}(X_t)$. The HMP includes three types of masks: 1) modality mask that randomly masks one modality. By modality mask, the encoder is encouraged to learn the information of the missing modality during reconstruction; 2) position mask, where positions are randomly selected, and the same positions are used to mask all the modalities; 3) patch mask complementarily selects patches of one position on different modalities. It forces the model to learn the semantic connection of each modality by reconstructing the masked patches.

The content information between different modalities of multi-modality MRI is highly coupled [27]. Image patches from different modalities at the same positions can be regarded as independent from each other. Therefore, the image patches can be masked or reserved independently. In this way, the content of the original image is maintained maximally while increasing the variance of the masked image, i.e., $\text{Var}(X_t)$. By increasing

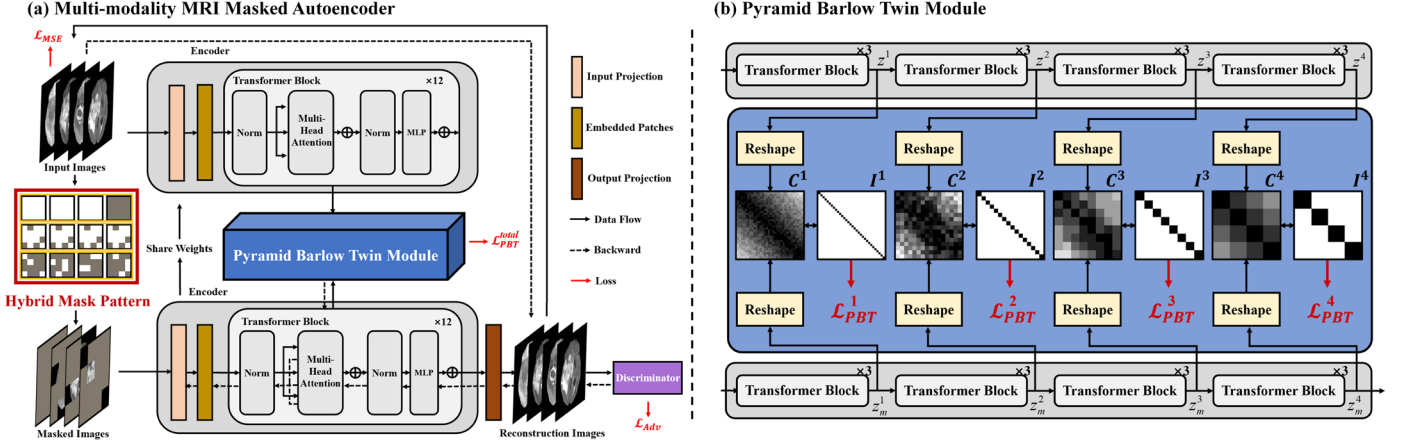


Fig. 4. (a) Overview of the proposed multi-modality MRI masked autoencoder (M^2 -MAE). The input images and masked images masked by HMP are fed to the share weights encoder respectively to reconstruct masked image for pre-training the encoder. (b) The detail of the pyramid barlow twin (PBT) module. The PBT module aims to align the semantic representations of input and masked images by implementing feature pyramid upon the encoder.

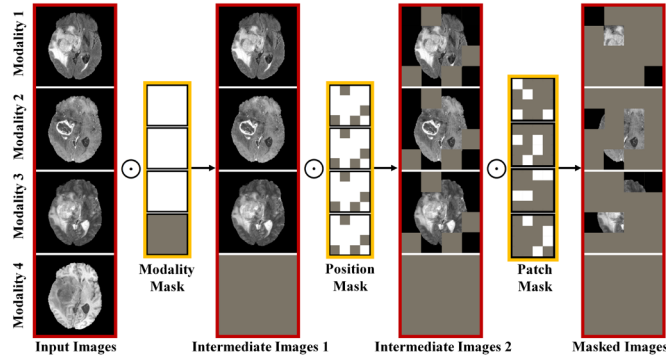


Fig. 5. Overview of the proposed masking strategy HMP. The input images are masked by HMP in three consecutive steps: 1) modality mask, 2) position mask, and 3) patch mask.

the $\text{Var}(X_i)$, the loss has a larger lower bound, and the self-supervised model is more resilient to collapse.

In addition, representations of multi-modality MRI by HMP masking can be better fused than other pretext tasks example [16]-[18], because learning the semantic connection among modalities can directly reconstruct the masked modality and image patches [41].

2) Pyramid Barlow Twin Module

The representations encoded by traditional MIM methods are not suitable for voxel-level dense prediction such as segmentation task because these methods do not consider different receptive field. This leads to misclassification of neighboring voxels of the same semantics into different categories. In recognition of this issue, a PBT module is designed and combined with HMP to further ensure stability of training and make pre-training weights suitable for segmentation and classification at different vision scale. To reconstruct the masked image patches by HMP at different vision scale and perform fine representation on downstream tasks, the PBT module aligns semantic representations between masked and original views in the pre-training stage. Let z^l and z_m^l be feature representations of the input and masked images, which are embedded by two encoders on layer l , respectively.

Specifically, the embedding is resized to the same level, then

calculate the cross-correlation matrix between embeddings from each encoder levels after being scaled to the same level can be calculated as:

$$C_{ij}^l = \frac{\sum z^{l,i} z_m^{l,j}}{\sqrt{\sum (z^{l,i})^2} \sqrt{\sum (z_m^{l,j})^2}} \quad (4)$$

where i and j index the vector dimension of the network output. C^l is a squared matrix at level l with element value ranging between -1 to 1.

The loss function \mathcal{L}_{PBT} follows:

$$\mathcal{L}_{PBT}^l = \sum_i (1 - C_{ii}^l)^2 + \sum_i \sum_{j \neq i} C_{ij}^l{}^2 \quad (5)$$

Intuitively, the invariance term of the objective, by trying to equate the diagonal elements of the cross-correlation matrix to 1, makes the embedding invariant to the masked applied. By trying to equate the non-diagonal elements of the cross-correlation matrix to 0, the redundancy reduction term decorrelates the different vector components of the embeddings to reduces the redundancy between output units. For the entire PBT module, the total loss is given by:

$$\mathcal{L}_{PBT}^{total} = \sum_l \mathcal{L}_{PBT}^l \quad (6)$$

3) Optimization

In summary, the M^2 -MAE is based on a MIM consisting of a PBT module and a discriminator to pre-train the encoder for multi-modality MRI datasets by reconstructing masked images. Given the multi-modality MR image x , the ViT encoder E_{ViT} and the output projection $g(\cdot)$, the MSE loss can be written as:

$$\mathcal{L}_{MSE} = \|x - g(E_{ViT}(x_m))\|^2 \quad (7)$$

The adversarial learning between generators (ViT Encoder and output projection) and discriminators forces the data distribution of the generated images to be close to that of the real images for each domain:

$$\mathcal{L}_{Adv} = \log(1 - D(g(E_{ViT}(x_m)))) + \log D(x) \quad (8)$$

Therefore, the overall M^2 -MAE is optimized by a joint loss function:

$$\mathcal{L}_{overall} = \mathcal{L}_{PBT}^{total} + \mathcal{L}_{MSE} + \mathcal{L}_{Adv} \quad (9)$$

C. Implementation Details

All of the models are implemented in PyTorch. MONAI is used for data transformation and loading. ViT-based architecture [16] is used as the standard encoder backbone. For the supervised baseline of the segmentation task, we employ a batch size of 4, the Adam optimizer, and a learning rate of 0.0003 with a weight decay of 0.05 based on a linear warmup-up to 300 epochs and a cosine annealing scheduler. Training is conducted on four NVIDIA 3090 GPU for a total of 1000 epochs.

Due to the differences between segmentation and classification tasks, different decoders are used for each task. For the segmentation tasks, UNETR [4] is adopted as the default supervised baseline in the study, which is one of the SOTA models in medical imaging segmentation. Specifically, UNETR is a U-shaped architecture employing a ViT as the encoder backbone and a convolutional upsampling decoder following the U-Net [2] design. For the classification tasks, self-supervised learning is widely used to evaluate the quality of pre-training by linear probing: the parameters of the encoder are fixed, and then a linear classifier is added to classify the images. Therefore, after adding the main encoder based on ViT, the projection head of one classification task is added as the classification header, the weights of the encoder are frozen and its pre-training, and the parameters of projection head are only updated under the fine-tune for the classification task.

IV. EXPERIMENTS

A. Datasets

1) BraTS2023

The multi-modality MR images of glioma patients are derived from the multi-modality brain tumor segmentation (BraTS2023) challenge [1]. Part of the BraTS2023 data belongs to The Cancer Imaging Archive, which can be available from the public repository. Genomic information was available from The Cancer Genome Atlas and IDH mutation status, FLAIR, T1, T1ce, and T2 modalities were assessed. For the glioma segmentation task, the final training dataset included 5004 preoperative MR images from 1251 subjects; the test dataset included 219 unlabeled subjects. Glioma segmentation was submitted to BraTS2023 to determine the segmentation accuracy for various algorithms. In the training dataset, only 369 subjects have IDH mutation, including 76 subjects with low-grade glioma (LGG) and 293 subjects with high-grade glioma (HGG). Thus, 299 subjects with IDH mutation status were used as training data, and 70 subjects with IDH mutation status are used as test data for IDH classification tasks.

2) PI-CAI

The full dataset used for the PI-CAI [42] public dataset comprises a cohort of 1500 prostate MRI exams, curated from three Dutch and one Norwegian center. Imaging consisted of the following sequences: axial T2-weighted imaging (T2W), diffusion-weighted imaging (DWI), and apparent diffusion coefficient maps (ADC). Out of the 1500 cases shared in the dataset, 1075 cases have International Society of Urological Pathology (ISUP) ≤ 1 , and 425 cases have ISUP ≥ 2 . The official

website also provides the segmentation labels on the transition zone (TZ) and peripheral zone (PZ). In the experiments, 1200 were used as training data and 300 subjects as test data by random data splitting.

3) Lung gas MRI

The LungasMRI acquisition is performed using the method previously reported by our group [31]. A total of 85 subjects were enrolled including 43 healthy volunteers and 42 patients with lung disease such as chronic obstructive pulmonary disease (COPD), asthma and so on. All subjects provided informed consents and the experiments were approved by the local Institutional Review Board (IRB). The parameters for ^1H imaging are as follows: repetition time/echo time (TR/TE) = 2.4/0.7 ms, matrix size = 96×96 , number of slices = 24. The parameters for ^{129}Xe imaging are as follows: TR/TE = 4.2/1.9 ms, matrix size = 96×96 , number of slices = 24. Professional doctors segmented the ^1H and ^{129}Xe images to obtain thoracic cavity mask and ventilation mask using ^1H and ^{129}Xe MR images. In the experiments, 68 subjects were used as training data and 17 subjects as test data by randomly data splitting.

B. Evaluation Metrics

To quantitatively evaluate the performance of the models on segmentation tasks, the Dice similarity score (Dice) and the 95% Hausdorff distance (HD95) are employed. For the classification tasks, area under the curve (AUC) and accuracy (Acc) are used for the quantitative evaluation.

C. Comparison With the SOTA Methods

Extensive experiments were conducted to compare the M^2 -MAE with state-of-the-art (SOTA) methods [3]-[8],[12],[18]-[20],[29],[43]-[45] on the three multi-modality datasets, as shown in Table I and Table II. To enable fair comparison, all the pre-training models adopted a Vision Transformer encoder with comparable parameters and were trained with the 3D images as input for pre-training, and the trained models were transferred to the downstream segmentation and classification tasks.

1) Reconstruction Task on Pre-training Stage

MAE[20], SimMIM[19] and M^2 -MAE were used to reconstruct masked multi-modality MRI in pre-training stage. Fig. 6 shows that MAE and SimMIM yielded reconstructed images with “averaging” effect of voxel signal intensities, which is similar to Fig. 1. However, our approach is capable of recovering high level semantic information such as the sharp contour of the brain and glioma. This suggests that M^2 -MAE mitigates model collapse in the pre-training stage and thus facilitates the downstream segmentation tasks.

2) Segmentation Task

The segmentation results are shown in Table I. The segmentation performance of the methods without pre-training is in the top rows. The segmentation performance of pre-training model is in the bottom rows. Experimental results show that the proposed model outperforms the comparative methods in the segmentation tasks. Particularly, the proposed M^2 -MAE achieves a mean Dice of 89.71%, 85.02%, 81.29% for the whole tumor (WT), tumor core (TC), enhancing tumor (ET) on

TABLE I
SEGMENTATION RESULTS OF THE PROPOSED METHOD AND OTHER EXISTING SOTA METHODS ON THREE MULTI-MODALITY DATASET

Schemes		BraTS2023 Dataset						PI-CAI Dataset		LungasMRI Dataset	
Method	Pre-train (w/o)	Dice (mean ± std) (%)			HD95 (mean ± std) (voxel)			Dice (mean ± std) (%)		Dice (mean ± std) (%)	
		WT	TC	ET	WT	TC	ET	TZ	PZ	TC	VD
3D UNet [3]	—	72.68±17.58	57.54±39.43	53.20±36.64	22.36±21.02	41.97±59.51	59.16±93.67	79.86±9.40	74.30±21.85	88.50±8.33	81.85±12.66
DMF Net [4]	—	79.18±15.74	61.70±37.18	58.67±31.85	21.53±25.97	37.38±52.11	48.37±87.96	83.25±9.81	73.94±18.04	90.77±9.76	82.08±11.80
nnUNet [5]	—	81.29±15.61	64.77±35.75	58.90±32.14	21.77±24.39	35.26±55.83	52.33±98.50	85.59±6.42	78.68±12.35	91.20±8.67	82.98±12.18
TransUNet [6]	—	85.84±13.93	81.61±22.57	76.63±26.57	12.35±28.32	8.91±17.38	19.68±55.50	87.72±7.30	81.72±6.42	93.25±4.88	87.92±8.52
TransBTS [7]	—	86.49±11.31	79.10±18.09	78.68±21.45	11.20±14.97	9.47±13.43	12.91±42.00	88.02±6.93	80.39±6.07	93.65±3.98	86.22±8.15
UNETR [8]	—	87.79±8.96	70.46±32.22	62.81±28.95	9.46±11.71	23.74±31.29	36.23±74.10	88.24±6.00	79.95±10.70	94.08±3.55	82.44±11.54
Moco [12]	✓	88.02±9.87	71.12±30.33	62.60±28.72	8.77±14.44	20.49±21.23	42.61±71.07	89.12±6.19	80.61±6.90	95.12±3.31	83.01±10.22
Barlow Twin [20]	✓	88.82±7.74	72.41±32.03	65.85±24.15	8.94±13.65	20.81±18.44	34.45±62.16	89.96±5.30	79.82±8.82	96.78±3.23	83.82±9.05
MAE [19]	✓	89.16±5.85	77.72±16.01	67.75±21.30	7.97±13.14	11.91±29.91	29.68±89.24	90.54±3.67	80.04±6.14	96.15±3.30	86.71±8.32
SimMIM [18]	✓	90.64±4.98	75.22±28.85	75.75±25.94	7.21±11.21	15.47±44.46	18.91±65.70	91.11±3.67	81.85±7.18	97.21±2.33	86.54±8.00
M ² -MAE(Ours)	✓	89.31±5.60	85.00±16.74	81.01±19.32	8.25±12.37	7.02±10.44	8.00±36.15	91.19±3.69	82.59±6.13	97.25±2.82	91.23±5.94

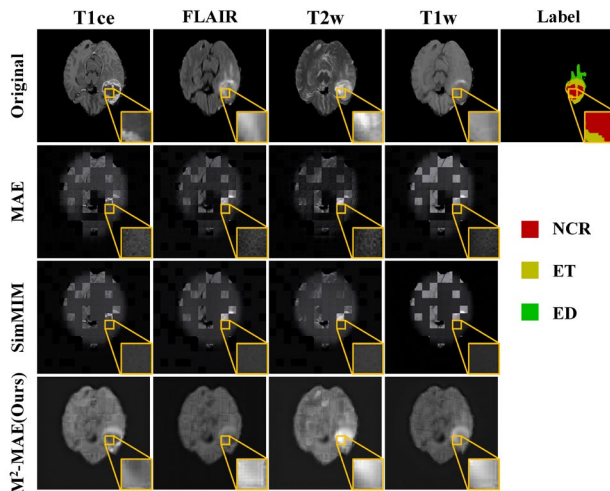


Fig. 6. Visual comparison of reconstructed results produced by different MIM methods for the BraTS2023 dataset. As the original images are all 3D volumes, reconstructed images are shown in the form of slices.

BraTS2023. The mean Dice for the transition zone (TZ) and peripheral zone (PZ) on PI-CAI are 91.19% and 82.59%, respectively, and the Dice for the thoracic cavity (TC) and ventilation defect (VD) region on LungasMRI is 97.25% and 91.23%, respectively. Most of the measurements obtained by the proposed method are the top among all the self-supervised segmentation methods. For the glioma segmentation task, the improvement in segmentation accuracy of TC and ET is most significant, with an increase of 14.56% and 18.48% in Dice compared to UNETR without pre-training. Furthermore, the qualitative results of M²-MAE and other comparison approaches in three datasets are shown in Fig. 7, Fig. 8, and Fig. 9 respectively. The proposed M²-MIM can produce more accurate segmentation results in most cases. Particularly, the edges of ET in Fig. 7 and TC in Fig. 9 are not misclassified, and the shape of PZ in Fig. 8 is complete.

3) Classification Task

The classification results are shown in Table II. It can be seen

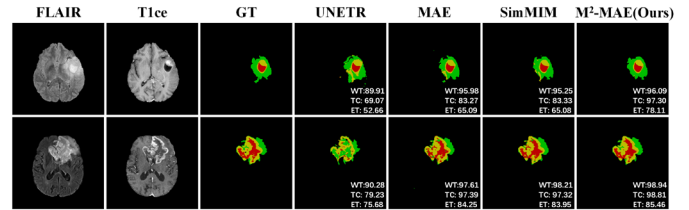


Fig. 7. Visual comparison of segmentation results produced by different methods for the BraTS2023 dataset. The glioma edema, tumor core and gangrene are presented in green, yellow, and red, respectively.

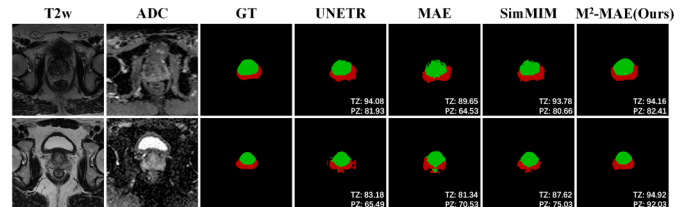


Fig. 8. Visual comparison of segmentation results produced by different methods for the PI-CAI dataset. The prostate transitional zone and zone of the prostate are presented in green and red, respectively.

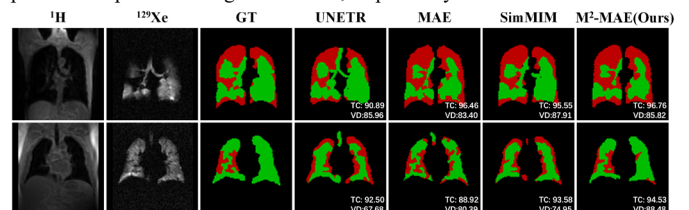


Fig. 9. Visual comparison of segmentation results produced by different methods for the LungasMRI dataset. The ventilation region and ventilation defect region are presented in green and red, respectively.

that the M²-MIM achieves remarkable classification performance for the classification task. Specifically, the M²-MAE achieved an AUC of 72.46% for IDH genotyping, 84.60% for prostate cancer grading, and 76.88% for lung disease classification. Compared with the SOTA pre-training methods, the proposed method achieves the best classification AUC. In addition, the model can approximate the supervised training model by training the classification head only, which reflects the good feature extraction ability.

TABLE II
CLASSIFICATION RESULTS OF THE PROPOSED METHOD AND OTHER EXISTING SOTA METHODS ON THREE MULTI-MODALITY DATASET

Schemes		BraTS2023 Dataset		PI-CAI Dataset		LungasMRI Dataset	
Method	Pre-train (w/o)	AUC (%)	Acc (%)	AUC (%)	Acc (%)	AUC (%)	Acc (%)
ResNet50[43]	—	76.42	73.91	86.52	83.67	78.69	70.59
SeNet101[44]	—	79.21	76.81	87.83	85.00	82.67	82.35
DenseNet121[29]	—	79.40	76.81	87.49	85.67	82.13	82.35
ViT [45]	—	80.04	79.71	91.28	90.33	88.91	88.24
Moco	✓	64.06	63.77	76.57	73.00	62.50	58.82
Barlow Twin	✓	68.38	65.22	78.28	76.33	60.63	58.82
MAE	✓	71.70	69.56	82.33	81.00	67.02	64.71
SimMIM	✓	70.50	68.12	83.52	81.67	68.38	64.71
M ² -MAE(Ours)	✓	72.46	71.01	84.60	82.00	78.88	70.59

To demonstrate the effects of the M²-MAE, the 2D features via t-SNE are shown in Fig. 10. Fig. 10 (a) and (b) show representations of test data on BraTS2023 and PI-CAI, respectively. Diseases of different grades are divided into two categories, although a few subjects are misclassified. Fig. 10 (c) shows representations of data on LungasMRI, where healthy subjects and patients with lung disease are divided into two categories without overlap. The distribution of the target features trained with the M²-MAE exhibits larger distance, suggesting the classification ability of self-supervised learning.

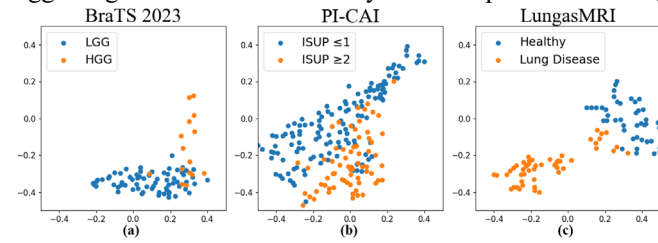


Fig. 10. 2D visualization of classification distributions using M²-MAE pre-training weights. (a) The subjects with LGG and HGG are presented in blue and red, respectively. (b) The subjects with ISUP ≤ 1 and ISUP ≥ 2 are presented in blue and red, respectively. (c) Healthy subjects and patients with lung disease are presented in purple and yellow, respectively.

4) Semi-supervised Segmentation Task

Based on dataset splitting, 20%, 40%, 60%, 80% and 100% of the labeled data are taken from the training data. Semi-supervised segmentation task is designed by using unlabeled data for M²-MAE pre-training and using labeled data for supervised segmentation training (shown in Fig. 11). The dashed line represents the result of experiments using all labeled data without M²-MAE pre-training weights. This exemplifies the potential impact of our approach in resource-constrained environments and its potential utility in field of multi-modality MRI analysis.

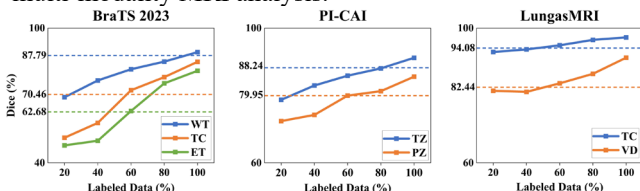


Fig. 11. An illustration of how M²-MAE advances the semi-supervised learning on segmentation task. 20%, 40%, 60%, 80%, and 100% labeled data are used to train the segmentation model with M²-MAE pre-training model.

D. Ablation Study

1) Evaluation of Masking Strategy

To demonstrate the effectiveness of the masking strategy, relevant ablation experiments are conducted. As shown in Table III, using the position mask and patch mask to reconstruct images during pre-training can effectively enhance the segmentation accuracy of TC and ET in BraTS2023, PZ in PI-CAI, and VD in LungasMRI. It has been indicated that, modality mask can improve the segmentation and classification accuracy of targets with different sizes, while patch mask can substantially improve the performance of small lesions.

TABLE III
EVALUATION OF PROPOSED MASKING STRATEGY ON THREE DATASETS

Mask Strategy			BraTS2023 Dataset			PI-CAI Dataset		LungasMRI Dataset				
Modality Mask	Position Mask	Patch Mask	Segmentation			Classify	Segmentation	Classify	Segmentation		Classify	
			Dice (mean) (%)			AUC (%)	Dice (mean) (%)		AUC (%)	Dice (mean) (%)		AUC (%)
			WT	TC	ET		TZ	PZ		TC	VD	
✓	✓	✓	87.52	71.08	63.21	64.51	89.20	80.73	82.72	94.78	82.48	67.01
			89.16	77.72	67.75	71.70	90.54	80.04	82.33	96.15	86.71	67.02
✓	✓	✓	88.61	80.54	70.56	70.66	90.14	82.92	83.21	96.09	88.67	67.06
			88.66	78.81	73.90	70.75	90.58	83.20	83.79	96.02	87.10	66.97
✓	✓	✓	89.55	80.17	77.29	71.77	90.32	82.99	84.27	97.03	88.72	67.34
			88.98	81.65	76.90	71.32	91.19	84.42	84.25	96.78	90.11	67.12
✓	✓	✓	89.06	83.41	80.19	70.06	90.75	84.44	84.27	96.54	89.91	67.00
			89.31	85.00	81.01	72.46	91.19	85.59	84.60	97.25	91.23	78.88

2) Evaluation of Pyramid Barlow Twin Module in Different Level

The proposed PBT module facilitates the model to learn the relationship between modalities and forces the encoders to learn reconstruction features at different vision scale. To analyze the effect of PBT at different levels, the scheme is adopted at each level in the pre-trained encoders. As shown in Table IV, the performance of the downstream tasks improves with levels and reaches the maximum at level=4. Considering the accuracy and quantity of training parameters, level = 4 is chosen as the optimal parameter of the number of transformer layers.

TABLE IV
EVALUATION OF M²-MAE USING PYRAMID BARLOW TWIN MODULE IN VARIOUS LEVEL

Level	BraTS2023 Dataset			PI-CAI Dataset		LungasMRI Dataset				
	Segmentation			Classify	Segmentation	Classify	Segmentation	Classify		
	Dice (mean) (%)			AUC (%)	Dice (mean) (%)		AUC (%)	Dice (mean) (%)	AUC (%)	
	WT	WC	ET		TZ	PZ		TC	VD	
1 (input)	88.81	84.14	80.76	71.27	90.87	85.22	84.09	96.83	90.99	74.49
2 (6 th , 12 th -layer)	88.85	84.51	80.81	71.71	90.81	85.28	84.02	96.01	91.12	74.70
3 (4 th , 8 th , 12 th -layer)	89.24	84.77	80.89	72.30	91.09	85.54	84.78	97.15	90.91	77.98
4 (3 rd , 6 th , 9 th , 12 th -layer)	89.31	85.00	81.01	72.46	91.19	85.59	84.60	97.25	91.23	78.88
12 (all layer)	89.70	83.15	79.50	69.54	90.24	83.45	83.71	96.66	90.60	67.11

3) Evaluation of Loss Function

To investigate the effects of proposed M²-MAE model, the quantitative results are presented in Table V. In comparison to the baseline in 1st row, the model with \mathcal{L}_{Dis} and \mathcal{L}_{PBT} gains an improvement in dice score of 1.34% for glioma segmentation.

These results indicate that \mathcal{L}_{Dis} and \mathcal{L}_{PBT} have complementary effects and can enhance the segmentation performances by improving the reconstruction accuracy of the pretext task during the pre-training stage.

TABLE V
EVALUATION OF PROPOSED LOSS FUNCTION ON THREE DATASETS

Loss function	BraTS2023 Dataset			PI-CAI Dataset			LungasMRI Dataset			
	Segmentation			Classify			Segmentation			Classify
	Dice(mean) (%)			AUC (%)	Dice(mean) (%)		AUC (%)	Dice(mean) (%)		AUC (%)
WT	WC	ET	TZ		PZ	TC		VD		
✓	88.26	83.07	79.96	68.11	90.72	84.41	83.51	96.87	89.10	68.07
✓ ✓	88.75	83.94	80.53	71.72	90.89	84.97	84.60	96.83	90.33	74.49
✓ ✓	89.07	84.45	80.76	69.78	91.05	85.29	83.55	97.20	90.91	67.44
✓ ✓ ✓	89.31	85.00	81.01	72.46	91.19	85.59	84.60	97.25	91.23	78.88

V. DISCUSSION

In this study, we deeply explore and analyze that the small lower bound of training loss induced by $\text{Var}(X_i)$ is the cause of model collapse in self-supervised training for multi-modality MRI. Based on this, we propose M^2 -MAE for multi-modality MRI self-supervised learning. We design a masking strategy HMP as the masking strategy to increase the lower bound of the training loss, providing a way to avoid model collapse and enhance the pre-training effect. In addition, we develop a PBT module to align the semantic representation of the original and masked image patches from HMP at different vision scales. Experiments show that M^2 -MAE can effectively avoid model collapse and enhance the pre-training performance and the accuracy of downstream segmentation and classification tasks.

The HMP directly improves the variance of masked images to reduce the risk of model collapse. Current self-supervised medical image analysis methods mostly treat multi-modality MRI as an indivisible whole and ignore the relationship between paired modalities. Although images from different modalities for the same sample present their exclusive features, they inherit some global content structures. For instance, the underlying anatomical structure of the brain is shared by all modalities in the BraTS2023 dataset. At present, the modality translation task has been proved to be beneficial for the segmentation tasks. It means reconstructing missing full modality or missing modality patches as the pretext task is significant for downstream tasks. For example, small lesion areas are easily missed by Vit-based encoders while effective improvement is achieved by mask reconstruction using a modality mask and patch mask (as shown in Table III). In addition, the HMP forces the model to explicitly capture correlations across different modalities, improving the robustness of model even with a small training dataset.

For HMP, we introduce a PBT module in M^2 -MAE to regularize the model by aligning the semantic representation at different vision scales in the latent space. In the PBT module, the performance of the downstream segmentation tasks is substantially enhanced with level=4. This may be due to the high efficiency of the parameter, which corresponds to the number of layers of jump connections in UNETR. However,

when the PBT was added to all the levels in the encoder, there was a noticeable decrease in the performance in the downstream classification/segmentation tasks, which may be attributed to the large number of training parameters that causes difficulties for the gradient to go backward.

We further evaluated the performance of M^2 -MAE by reducing the amount for labeled data. Fig. 11 demonstrates the comparison results of fine-tuning using a subset of three datasets. Using only 60% labeled dataset for supervised training, experiments with M^2 -MAE pre-training weights achieved similar performance compared to training from scratch on small regions like TC, ET, PZ, and VD. Our findings suggest promising future implications and potential extensions of this work for other medical imaging tasks. Compared with traditional semi-supervised learning, consistency-based semi-supervised is built on a consistent data distribution, which may not suit datasets from multiple data centers. Pseudo label-based semi-supervised learning methods may produce error amplification and increase the risk of training instability. In contrast, the self-supervised learning is used to learn universal features through a pretext task, which can reduce errors from data bias.

We acknowledge several study limitations. For example, regarding the generality of the method to different tasks, the Modality Mask strategy in the HMP randomly masks a whole modality for the input multi-modality MRI. However, each modality has different importance for the downstream tasks, e.g. the T1ce is more important compared to T1 for the glioma segmentation task. The adoption of the proposed mask strategy for use in specific lesions, organs, and downstream tasks warrants further refinement.

VI. CONCLUSION

In this work, the M^2 -MAE is developed to enhance SSL by preventing model collapse for multi-modality MRI segmentation and classification. The HMP masks the multi-modality MRI on three different levels and can directly improve the variance of masked images and learn the semantic connections of multi-modality images. In the pre-training stage, the PBT module aligns the semantic representation of image patches in latent space using a pyramidal hierarchy of Barlow Twin loss. Experiments showed that our proposed approach improves the performance of the downstream tasks and achieves similar performance to a fully supervised model using 60% of label. This approach provides a reliable strategy for exploiting unlabeled data to steadily enhance the performance of downstream segmentation and classification tasks, lending support to import clinical diagnosis and treatment efficacy of small lesions.

REFERENCES

- [1] B. H. Menze *et al.*, "The multimodal brain tumor image segmentation benchmark (BRATS)," *IEEE Trans. Med. Imaging*, vol. 34, no. 10, pp. 1993-2024, Oct. 2015.
- [2] O. Ronneberger, P. Fischer, and T. Brox, "U-Net: Convolutional networks for biomedical image segmentation," in *Medical Image Computing and Computer Assisted Intervention (MICCAI)*, Oct. 2015, pp. 234-241.

- [3] Ö. Çiçek, A. Abdulkadir, S. S. Lienkamp, T. Brox, and O. Ronneberger, "3d u-net: Learning dense volumetric segmentation from sparse annotation," in *Medical Image Computing and Computer Assisted Intervention (MICCAI)*, Oct. 2016, pp. 534.
- [4] C. Chen, X. Liu, M. Ding, J. Zheng, and J. Li, "3D dilated multi-fiber network for real-time brain tumor segmentation in MRI," in *Medical Image Computing and Computer Assisted Intervention (MICCAI)*, Oct. 2016, pp. 184-192.
- [5] F. Isensee, P. F. Jaeger, S. A. Kohl, and Petersen, "nnU-Net: a self-configuring method for deep learning-based biomedical image segmentation," *Nature Methods*, vol. 18, no. 2, pp. 203-211, Dec. 2021.
- [6] J. Chen *et al.*, "Transunet: Transformers make strong encoders for medical image segmentation," *arXiv preprint arXiv:2102.04306*, 2021.
- [7] W. Wang *et al.*, "Transbts: Multimodal brain tumor segmentation using transformer," in *Medical Image Computing and Computer Assisted Intervention (MICCAI)*, Sep. 2021, pp. 109-119.
- [8] A. Hatamizadeh *et al.*, "UNETR: Transformers for 3D medical image segmentation," in *IEEE/CVF Winter Conference on Applications of Computer Vision (WACV)*, Jan. 2022, pp. 1748-1758.
- [9] R. Zheng *et al.*, "MsVRL: Self-supervised multiscale visual representation learning via cross-level consistency for medical image segmentation," *IEEE Trans. Med. Imaging*, vol. 42, no. 1, pp. 91-102, Jan. 2023.
- [10] Chen. Z *et al.*, "C-CAM: Causal CAM for weakly supervised Semantic Segmentation on Medical Image," in *IEEE Conference on Computer Vision and Pattern Recognition (CVPR)*, Jun. 2022, pp. 11676-11685.
- [11] T. Chen, S. Kornblith, M. Norouzi, and G. Hinton, "A simple framework for contrastive learning of visual representations," in *International Conference on Machine Learning (ICML)*, Jul. 2020.
- [12] K. He, H. Fan, Y. Wu, S. Xie, and R. Girshick, "Momentum contrast for unsupervised visual representation learning," in *IEEE Conference on Computer Vision and Pattern Recognition (CVPR)*, Jun. 2020.
- [13] M. Caron, I. Misra, J. Mairal, P. Goyal, P. Bojanowski, and A. Joulin, "Unsupervised learning of visual features by contrasting cluster assignments," in *Neural Information Processing Systems (NeurIPS)*, Dec. 2020, pp. 9912-9924.
- [14] J.-B. Grill *et al.*, "Bootstrap your own latent - A new approach to self-supervised learning," in *Neural Information Processing Systems (NeurIPS)*, Dec. 2020, pp. 21271-21284.
- [15] X. L. Chen, and K. M. He, "Exploring simple siamese representation learning," in *IEEE Conference on Computer Vision and Pattern Recognition (CVPR)*, Jun. 2021, pp. 15745-15753.
- [16] H. Bao, L. Dong, S. Piao, and F. Wei, "BEiT: BERT pre-Training of image Transformers," in *International Conference on Machine Learning (ICML)*, Apr. 2022.
- [17] J. Zhou, C. Wei, H. Wang, W. Shen, C. Xie, A. Yuille, and T. Kong, "Image BERT pre-training with online tokenizer," in *International Conference on Machine Learning (ICML)*, Apr. 2022.
- [18] Z. Xie, Z. Zhang, Y. Cao, Y. Lin, J. Bao, Z. Yao, Q. Dai, and H. Hu, "Simmim: A simple framework for masked image modeling," in *IEEE Conference on Computer Vision and Pattern Recognition (CVPR)*, Jun. 2022, pp. 9643-9653.
- [19] K. M. He, X. L. Chen, S. N. Xie, Y. H. Li, P. Dollár, and R. Girshick, "Masked autoencoders are scalable vision learners," in *IEEE Conference on Computer Vision and Pattern Recognition (CVPR)*, Jun. 2022, pp. 15979-15988.
- [20] J. Zbontar, L. Jing, I. Misra, Y. LeCun, and S. Deny, "Barlow Twins: Self-supervised learning via redundancy reduction," in *International Conference on Machine Learning (ICML)*, Jun. 2021, pp. 12310-12320.
- [21] Z. K. Chen *et al.*, "Masked image modeling advances 3D medical image analysis," in *IEEE/CVF Winter Conference on Applications of Computer Vision (WACV)*, Jul. 2023, pp. 1969-1979.
- [22] Shuhao Cao, Peng Xu and David A. Clifton "How to understand masked autoencoders," *arXiv preprint arXiv:2202.03670*, 2022.
- [23] Q. Zhang, Y. Wang, and Y. Wang, "How mask matters: Towards theoretical understandings of masked autoencoders," in *Neural Information Processing Systems (NeurIPS)*, Dec. 2022, pp. 27127-27139, 2022.
- [24] X. Yan *et al.*, "Representation recovering for self-supervised pre-training on medical images," in *IEEE/CVF Winter Conference on Applications of Computer Vision (WACV)*, Jul. 2023, pp. 2684-2694.
- [25] P. Schelb *et al.*, "Comparison of prostate MRI lesion segmentation agreement between multiple radiologists and a fully automatic deep learning system," *ROFO-FORTSCHR RONTG*, vol. 193, no. 05, pp. 559-573, May. 2021.
- [26] N. Wang *et al.*, "MISSU: 3D medical image segmentation via self-distilling TransUNet," *IEEE Trans. Med. Imaging*, vol. 42, no. 9, pp. 2740-2750, Sep. 2023.
- [27] Q. Yang, X. Guo, Z. Chen, Peter Y.M. Woo and Y. Yuan, "D2-Net: Dual disentanglement network for brain tumor segmentation with missing modalities," *IEEE Trans. Med. Imaging*, vol. 41, no. 10, pp. 2953-2964, Oct. 2022.
- [28] Q. Chen *et al.*, "Modality-specific information disentanglement from multi-parametric MRI for breast tumor segmentation and computer-aided diagnosis," *IEEE Trans. Med. Imaging*, Jan. 2024.
- [29] S. Liang *et al.*, "Multimodal 3D DenseNet for IDH genotype prediction in gliomas," *Genes*, vol. 9 no. 8, pp. 382, Jul. 2018.
- [30] J. H. Cheng, J. Liu, H. L. Kuang, and J. X. Wang, "A fully automated multimodal MRI-based multi-task learning for Glioma segmentation and IDH genotyping," *IEEE Trans. Med. Imaging*, vol. 41, no. 6, pp. 1520-1532, Jun. 2022.
- [31] Z. Li *et al.*, "Complementation-reinforced network for integrated reconstruction and segmentation of pulmonary gas MRI with high acceleration," *Medical Physics*, vol. 51 no. 1, pp. 378-393, Jul. 2023.
- [32] M. Bencevic, M. Habijan, I. Galic, and A. Pizurica, "Self-supervised learning as a means to reduce the need for labeled data in medical image analysis," in *European Signal Processing Conference (EUSIPCO)*, Aug. 2022, pp. 1328-1332.
- [33] H.-Y. Zhou, C. Lu, S. Yang, X. Han, and Y. Yu, "Preservational learning improves self-supervised medical image models by reconstructing diverse contexts," in *International Conference on Computer Vision (ICCV)*, Oct. 2021, pp. 3479-3489.
- [34] J. Yankai *et al.*, "Anatomical invariance modeling and semantic alignment for self-supervised learning in 3D medical image analysis," in *International Conference on Computer Vision (ICCV)*, Oct. 2023, pp. 15859-15869.
- [35] R. Yan *et al.*, "Label-efficient self-supervised federated learning for tackling data heterogeneity in medical imaging," *IEEE Trans. Med. Imaging*, vol. 42, no. 7, pp. 1932-1943, Jul. 2023.
- [36] F. Haghghi *et al.*, "DiRA: Discriminative, restorative, and adversarial learning for self-supervised medical image analysis," in *IEEE Conference on Computer Vision and Pattern Recognition (CVPR)*, Jun. 2022, pp. 20792-20802.
- [37] S. F. Zhang *et al.*, "Align representations with base: A new approach to self-supervised learning," in *IEEE Conference on Computer Vision and Pattern Recognition (CVPR)*, Jun. 2022, pp. 16579-16588.
- [38] F. Wang, T. Kong, R. Zhang, H. Liu, and H. Li, "Self-supervised learning by estimating twin class distribution," *IEEE Trans. Image Process*, vol. 32, pp. 2228-2236, Apr. 2023.
- [39] S. Moon, D. Buracas, S. Park, J. Kim, and J. Canny, "An embedding-dynamic approach to self-supervised learning," in *IEEE/CVF Winter Conference on Applications of Computer Vision (WACV)*, Jul. 2023, pp. 2749-2757.
- [40] A. Krizhevsky, "Learning multiple layers of features from tiny images," M.S. thesis, Dept. Comput. Sci., Univ. Toronto, Toronto, ON, Canada, 2009.
- [41] L. Shen *et al.*, "Multi-domain image completion for random missing input data," *IEEE Trans. Med. Imaging*, vol. 40, no. 4, pp. 1113-1122, Apr. 2021.
- [42] A. L. Abreu *et al.*, "PROSTATEx Challenges for computerized classification of prostate lesions from multiparametric magnetic resonance images," *Journal of Medical Imaging*, vol. 5 no 4, pp. 044501, Oct. 2018.
- [43] K. Chang, H. X. Bai, H. Zhou, and C. Su, "Residual convolutional neural network for the determination of IDH status in low- and highgrade gliomas from MR imaging," *Clin. Cancer Res.*, vol. 24, no. 5, pp. 1073-1081, Mar. 2019.
- [44] J. Hu, L. Shen, and G. Sun, "Squeeze-and-excitation networks," in *International Conference on Computer Vision (ICCV)*, Jun. 2018, pp. 7132-7141.
- [45] A. Dosovitskiy *et al.*, "An image is worth 16x16 words: Transformers for image recognition at scale," in *International Conference on Learning Representations (ICLR)*, May. 2021.